Journal of
Materials Chemistry C

ROYAL SOCIETY
OF CHEMISTRY

PAPER

View Article Online
View Journal | View Issue

Check for updates

Cite this: *J. Mater. Chem. C*, 2025, **13**, 13415

Cr^{3+}-doped $CaMgGe_2O_6$ phosphors: crystal field effects and the synergistic role of FIR and fluorescence lifetime in multi-mode optical thermometry†

Yosra Bahrouni,[a] Ikhlas Kachou,[a] Kamel Saidi,[ab] Christian Hernández-Álvarez,[cd] Mohamed Dammak *[a] and Inocencio R Martín[c]

Received 21st March 2025,
Accepted 19th May 2025

DOI: 10.1039/d5tc01229e

rsc.li/materials-c

Luminescence thermometry has attracted growing interest for its potential in remote and non-contact temperature sensing. Among luminescent ions, Cr^{3+} is widely studied for optical thermometry using fluorescence intensity ratio (FIR), but its fluorescence lifetime (FL) thermometric potential remains largely undiscovered. In this study, we present a detailed spectroscopic investigation of Cr^{3+}-doped $CaMgGe_2O_6$, demonstrating the complementary advantages of FIR and FL-based thermometry. X-Ray diffraction (XRD) confirms the monoclinic phase with high crystallinity, while diffuse reflectance spectroscopy provides insight into the crystal field strength ($D_q/B \approx 1.81$) and optical band gap (E_g). Under 405 nm excitation, we systematically analyze the photoluminescence and temperature-dependent luminescence behavior. The multi-mode thermal sensing approach reveals that FIR (I_{589}/I_{771}) achieves a remarkable maximum sensitivity of 1.4% K^{-1} at 390 K, with an exceptionally low temperature uncertainty ($\sim$0.11 K at room temperature), establishing its reliability for precise temperature detection. Meanwhile, FL thermometry exhibits an even higher maximum sensitivity of 2.5% K^{-1} at 478 K, underscoring its strong potential as an alternative or complementary technique. By integrating both methods, we achieve enhanced accuracy, broader temperature coverage, and improved adaptability to various sensing environments. This work highlights the first comprehensive demonstration of FL-based thermometry in Cr^{3+}-doped phosphors, paving the way for optimized multi-mode luminescent thermal sensors and reinforcing the critical role of both the host matrix and advanced spectroscopic characterization.

Introduction

Luminescence thermometry has received considerable attention recently and is becoming a rapidly growing field of nanotechnology, particularly for temperature measurement in remote sensing.[1–3] This technique relies on the luminescence properties of phosphors, such as spectral shape, emission intensity, or the kinetics of excited states of incorporated dopants, enabling fast and accurate real-time temperature measurement with sub-micrometer spatial and millikelvin thermal resolution.[4,5] These characteristics make luminescence thermometry a valuable complement to thermal imaging cameras, which only provide surface temperature maps.

Among various luminescence thermometry approaches, the fluorescence intensity ratio (FIR) method is widely employed due to its self-referencing nature. Systems with two exciting states in thermal equilibrium (strongly thermodynamically coupled) offer high selectivity with respect to temperature. In such systems, the population distribution between thermally coupled states follows the Boltzmann law, ensuring a rapid renormalization of the emission intensity when external factors influence the overall quantum yield.[6,7] For biological applications, an ideal FIR-based optical thermometer requires a single-doped material with two thermally coupled excited states that can be efficiently excited and emit within the biological optical windows, where tissue absorption and scattering are minimized.[8,9] Another widely used luminescence thermometry technique is fluorescence lifetime (FL) thermometry, which is independent of external

---

[a] *Laboratoire de Physique Appliquée, Faculté des Sciences de Sfax, Département de Physique, Université de Sfax, BP 1171, Sfax, Tunisia. E-mail: madidammak@yahoo.fr, mohamed.dammak@fss.usf.tn*

[b] *Department of Physics, Sfax Preparatory Engineering Institute, University of Sfax, 1172 – 3000, Sfax, Tunisia*

[c] *Universidad de La Laguna, Departamento de Física, MALTA-Consolider Team, IMN and IUdEA Apdo. Correos 456, E-38206, San Cristóbal de La Laguna, Santa Cruz de Tenerife, Spain*

[d] *Adam Mickiewicz University, Faculty of Chemistry, Uniwersytetu Poznańskiego 8, 61-614, Poznań, Poland*

† Electronic supplementary information (ESI) available. See DOI: https://doi.org/10.1039/d5tc01229e

influences and relies on measuring the temperature-dependent luminescence lifetime of excited states.[10,11] Combining FIR and FL methods enhances the accuracy and reliability of temperature measurements by providing complementary information: FIR ensures high sensitivity in a specific range, while FL extends the measurable temperature range and improves robustness against fluctuations in the excitation power or concentration.

For the development of highly sensitive phosphors, the choice of a stable host material and an appropriate activator with thermally coupled levels is crucial. While phosphate,[12,13] borate,[14,15] and silicate[16–18] luminescent materials have been extensively studied, germanate hosts have received comparatively less attention. However, germanate compounds offer advantages such as high thermal and chemical stability, hardness, and broad transparency. Furthermore, they exhibit the ability to generate deep red emissions in the desired wavelength range under UV and blue excitation.[19] The crystal structure of germanates varies despite their similar chemical formulas, primarily due to differences in the size of monovalent and divalent cations, which influence bond lengths and the crystal field strength.[20–22]

The performance of inorganic luminescent materials is determined by the combination of the host lattice and the activator ions. Rare earth and transition metal ions have been widely investigated as activators for near-infrared (NIR) emission. However, a major challenge in NIR-emitting materials is the enhancement of the photoluminescence quantum yield, particularly for 4f–4f transitions in lanthanide ions.[23–25] Chromium ions (Cr^{3+}), with a $3d^3$ valence electron configuration, are attractive alternatives due to their strong crystal field interactions and tunable luminescence properties.[26] Unlike the 4f orbitals of lanthanides, the 3d electrons of Cr^{3+} interact strongly with the surrounding crystal field, leading to well-defined energy level splitting, including the $^4A_{2g}$, ^2E, $^2T_{1g}$, and $^4T_{2g}$ states.[27] The relative positioning of the ^2E and $^4T_2$ states is highly dependent on the crystal field strength, which directly affects the emission characteristics.[1] Because of these properties, Cr^{3+} is commonly doped into various inorganic hosts for laser and luminescence applications.

Germanate-based host materials provide a weaker crystal field environment for Cr^{3+} ions compared to silicates, leading to red-shifted emission with potential applications in luminescence thermometry. In this study, $CaMgGe_2O_6$ was selected as a host matrix, with Cr^{3+} as the activator, to develop a novel series of $CaMgGe_2O_6$:0.01Cr^{3+} (CMGO:0.01Cr^{3+}) luminescent materials.

In this work, we investigate the luminescence thermometric properties of Cr^{3+}-doped $CaMgGe_2O_6$ (CMGO:Cr^{3+}) as a potential dual-mode optical thermometer. The study explores the structural, optical, and thermal characteristics of the synthesized phosphors, focusing on their ability to function as a reliable temperature sensor. By combining fluorescence intensity ratio (FIR) and fluorescence lifetime (FL) techniques, we aim to assess the potential of CMGO:0.01Cr^{3+} for accurate and robust temperature measurements. The influence of the crystal field environment on the luminescence properties of Cr^{3+} ions is analyzed to understand its impact on thermometric performance. This work provides insights into the design of non-lanthanide-based luminescent thermometers and their applicability in advanced temperature sensing.

Experimental section

Sample preparation

The chemical composition of CMGO:0.01Cr^{3+} was successfully synthesized by a high temperature solid-state reaction method. The crude reagents $CaCO_3$, GeO_2, MgO and Cr_2O_3 were used without further purification. Stoichiometric amounts of the starting materials were first thoroughly mixed by grinding in an agate mortar and presintered at 800 °C for 8 h in air. After complete grinding, the presintered samples were then sintered at a higher temperature of 1200 °C for 5 hours in air. Finally, the samples were allowed to cool naturally to room temperature in an oven and then ground into powders for further characterization.

Characterization

The X-ray diffraction (XRD) patterns of phosphorus were obtained at room temperature using a Bruker D8-Advance powder X-ray diffractometer. Monochromatic CuKa1 copper radiation (1.5406 Å) was used in the 2θ range (20–80°). The morphology of the samples was analyzed using a Zeiss Supra55VP FEG-SEM and a Bruker XFlash 5030. For the determination of the UV-vis-NIR absorption, a UV-vis-NIR spectrometer (PerkinElmer Lambda 365) was used.

A high-resolution CCD detector (Avantes) was used to detect the emission spectra. Spectra Physics 3900S was used for 405 nm excitation and a Linkam (THMS600) for sample heating. Decay curves were obtained using a 200 MHz LeCroy WS424 oscilloscope, a Hamamatsu R928 photomultiplier tube (PMT), and a tunable EKSPLA/NT342/3/UVE 10 ns pulsed laser (optical parametric oscillator – OPO) operated at a repetition rate of 10 Hz as the excitation source.

Results and discussion

Structural and morphological analysis of the obtained materials

To confirm their composition and morphology, the synthesized particles were subjected to extensive analysis. X-Ray powder diffraction measurements showed that the synthesized sample was composed of a single phase, with no occurrence of appearance phases. The XRD patterns, both experimental and calculated by Rietveld refinement, are shown in Fig. 1a for CMGO:0.01Cr^{3+}. The structural data given in ref. 28 were used as the starting model for the Rietveld calculations. There was good agreement between the experimental and calculated patterns, resulting in satisfactory fit factors. The monoclinic system and the space group $C2/c$ were confirmed.[29] Table S1 (ESI†) shows a summary of the structural parameters derived from the Rietveld refinement of the samples illustrated.

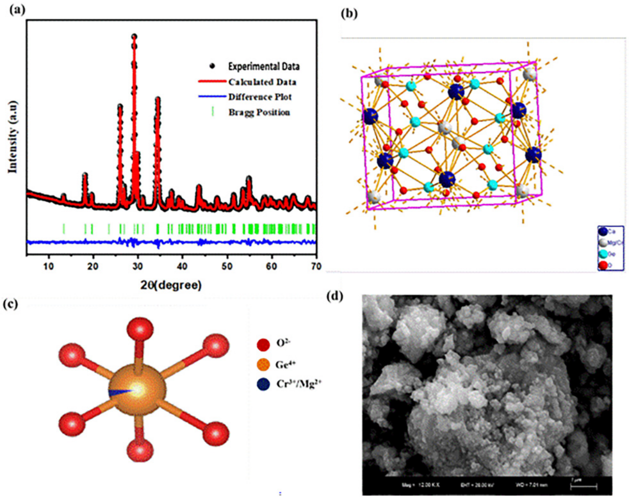

Fig. 1 (a) Rietveld refinement of XRD patterns. (b) Visual crystal structure. (c) The potential occupancies of doped ions in a polyhedron. (d) SEM image of the CMGO:0.01Cr^{3+} sample.

Depending on these experimental results, the crystal structure of $CaMgGe_2O_6$ is depicted in Fig. 1b. It is made up of [CaO_8] dodecahedrons, [MgO_6] octahedrons and [GeO_4] tetrahedrons. Each type of polyhedron is linked by common oxygen atoms to form an infinite chain parallel to the *c*-axis. Consider the ionic radii of Ca^{2+} (1.12 Å, coordination number (CN) = 8), Mg^{2+} (0.72 Å, CN = 6), Ge^{4+} (0.39 Å, CN = 4) and Cr^{3+} (0.615 Å, CN = 6).[30] Since the appearance of the emission spectra of this transition metal ion is sensitive to changes in the crystal field strength, this can strongly influence the spectroscopic properties of the Cr^{3+} ions. In accordance with the above description, Cr^{3+} ions could be substitutes for Mg^{2+} ions (polyhedral representation), as shown in Fig. 1c. In addition, the energy difference between the electron configuration of the particular ligand field and the isotropic field is referred to as the crystal field stabilization energy (CFSE). The CFSE is large for ions with an electronic configuration of d^3 and d^8 ions in the octahedral ligand, so the Cr^{3+} site has a preference for octahedral sites. Thus, we suggest that Cr^{3+} ions substitute for Mg^{2+} to form [CrO_6] octahedrons.[31]

The size of the individual particles formed is generally in the micrometer range (~1 μm) as shown by the SEM images of the synthesized luminophores (Fig. 1d). The agglomerated morphology with a broad size distribution is achieved using solid-state synthesis.

Optical characterization

UV-visible diffuse reflectance analysis. The UV-visible diffuse reflectance spectrum of the sample was measured in the 200–800 nm range and is illustrated in Fig. S2a (ESI†). The absorption band at 245 nm is due to the band-to-band transition of CMGO. The absorption edges at 403 and 533 nm are attributed to the Cr^{3+} d–d transition.[32] The diffuse reflectance spectra are used to estimate the optical band gap of the phosphors using the Tauc formula and Kubelka–Munk theory. This is done by converting the reflectance to the Kubelka–Munk function using the following relation.[33,34]

$$F(R) = \frac{(1-R)^2}{2R} = \frac{K}{S} \tag{1}$$

where *R* is the spectral diffuse reflectance and *K* and *S* are the absorption and scattering coefficients. The Tauc formula for the direct band gap is obtained using

$$\alpha h\nu = c(h\nu - E_g)^{1/2} \tag{2}$$

where $h\nu$ is the energy of the emitted photon, α is the absorption coefficient, *c* is a constant, and E_g is the band gap. The Kubelka–Munk function can be calculated by replacing α by $F(R_\infty)$. The plot of the $[h\nu(R_\infty)]^2$ as a function of $h\nu$ is used to obtain the bandgap. As can be seen in Fig. S2b (ESI†), the bandgap value obtained (~4.25 eV) is close to the reported bandgap values for CMGO, confirming that it is a wide bandgap semiconductor.[35]

Luminescence properties and crystal field analysis: the Tanabe–Sugano diagram. The photoluminescence excitation (PLE) spectrum by monitoring the emission intensity at 704 nm of CMGO:0.01Cr^{3+} was measured (Fig. 2a). There are two absorption bands in the PLE spectrum, peaking at 427 and 589 nm, which should be attributed to the spin-allowed

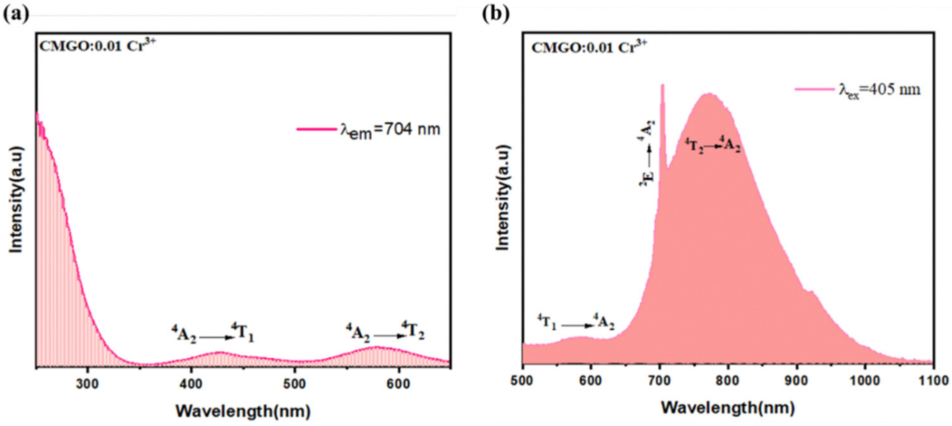

Fig. 2 (a) Excitation spectrum when monitoring the emission at 704 nm. (b) Emission spectrum upon excitation at 405 nm of CMGO:0.01Cr^{3+}.

transitions ${}^4A_{2g} \rightarrow {}^4T_{1g}$ (${}^4F$) and ${}^4A_{2g} \rightarrow {}^4T_{2g}$ (${}^4F$).[36,37] Upon 405 nm excitation, the PL emission spectrum is composed of three sharp luminescence lines due to the ${}^4T_1 \rightarrow {}^4A_2$ transitions at 589 nm,[38] the spin-forbidden ${}^2E \rightarrow {}^4A_2$ transitions (R-lines) at 696 and 704 nm and a broad luminescence band centered at about 771 nm due to the spin-allowed electronic transition from the excited state ${}^4T_{2g}$ (${}^4F$) to the ground state ${}^4A_{2g}$ (${}^4F$), as shown in Fig. 2b.[39,40]

Furthermore, it is well known that the R line of the Cr^{3+} zero phonon is mainly affected by the side band vibration. It is noteworthy that the anti-Stokes (696 nm) disappears in the PL spectra, while the Stokes remains at 704 nm. The red shift of the PL is related to the variation of the crystal field according to previous work.[41] This indicates that the crystal field was weakened by the stretching of the Cr–O bonds. The estimation of the crystal field (D_q) and the ray parameter (B), using the Tanabe–Sugano diagram shown in Fig. 3b, in the crystal conditions is given by using the following formula:[42,43]

$$\Delta E = E({}^4A_2 \rightarrow {}^4T_1) - E({}^4A_2 \rightarrow {}^4T_2) \tag{3}$$

$$\Delta S = E({}^4A_2 \rightarrow {}^4T_1) - E({}^4A_2 \rightarrow {}^4T_2) \tag{4}$$

$$10 \times D_q = E({}^4A_2 \rightarrow {}^4T_2) - \frac{\Delta S}{2} \tag{5}$$

$$\frac{D_q}{B} = \frac{15(x-8)}{x^2 - 10x} \tag{6}$$

$$x = \frac{\Delta E}{D_q}$$

where B is the Racah parameter, D_q is the crystal field splitting energy, ΔE is the energy difference between ${}^4A_2 \rightarrow {}^4T_1$ and ${}^4A_2 \rightarrow {}^4T_2$ based on the PLE spectrum, and ΔS is the Stokes shift, which can be calculated from the excitation band of ${}^4A_2 \rightarrow {}^4T_2$ and the emission band of ${}^2E \rightarrow {}^4A_2$. In agreement with previous relations are the estimated values of B = 685 cm^{-1}, D_q = 1254 cm^{-1} and D_q/B = 1.84. Thus, the Cr^{3+} ions are located in a weak crystalline field in the CMGO host, a case where sharp and broader peaks coexist. If the Cr^{3+} ions were in a weak crystal field, the energy interval between the ground (${}^4A_2$) and excited states (${}^4T_1$ and ${}^4T_2$) would be smaller, resulting in a red shift in the Cr^{3+} d–d transition. Indeed, the intensity of the crystal field is strongly influenced by variations of the cation–oxygen–anion distance caused by lattice vibrations, defects and local structure distortions.[44,45]

To further study this mechanism, we explain thermal quenching on the basis of conformational coordinates as follows. The luminescence spectra of Cr^{3+}-doped materials result from d–d electronic transitions; in the case of transition metals with the 3d^3 electronic configuration observed for Cr^{3+}, depending on the intensity of the crystal field of the host material, the spectrum is dominated either by a narrow ${}^2E \rightarrow {}^4A_2$ emission band (strong crystal field) or by a broad ${}^4T_2 \rightarrow {}^4A_2$ emission band for the weak crystal field (Fig. 3a). Bearing in mind, the fact that the analyzed structures contain perfect octahedral sites of Mg^{2+}/Ca^{2+} ions the observed changes in the shape of the emission spectra and the gradual increase in the intensity of the ${}^4T_2 \rightarrow {}^4A_2$ band relative to the ${}^2E \rightarrow {}^4A_2$ band can be directly correlated with the change in the strength of the crystal field resulting from the extension of the Cr^{3+}–O^{2-} bond length.[46,47]

Temperature dependence of the PL spectra

The temperature-dependent PL emission spectra of the Cr^{3+}-doped CMGO system were analyzed with the dual aim of

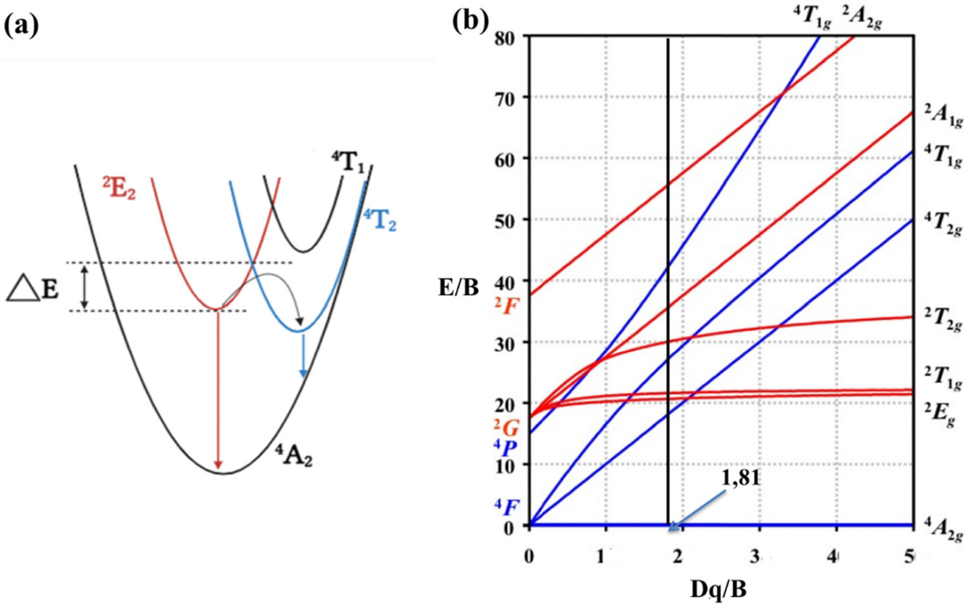

Fig. 3 (a) Schematic configurational coordinate diagram. (b) Tanabe–Sugano energy level diagram in which the straight lines indicate the crystal fields of the CMGO:0.01Cr^{3+} samples.

analyzing the thermal response and investigating in detail the electronic configuration and the parameters describing the coupling with the phonon lattice. The spectra in Fig. 4a show the strong thermal quenching of the system with increasing temperature. The trend shows a strong decrease of the broad emission of $^4T_2$ with respect to the spin-forbidden R-line emission with increasing temperature, The extinction temperature is in the range of 298–450 K according to the integrated PL intensity trend $^4T_2$, suggesting a thermally activated process between the excited states.[48]

With a further increase in temperature from 298 K to 450 K, the emission intensity of CMGO:0.01Cr^{3+} gradually decreases for the levels ($^4T_2 \rightarrow {}^4A_2$) but gradually increases for the levels ($^4T_1 \rightarrow {}^4A_2$), showing an opposite temperature dependence. Moreover, the latter considers the background contribution to the signal from other emission processes. The trend shows a strong decrease of the broad emission of $^4T_2$ with respect to the spin-forbidden R-line emission with increasing temperature, suggesting a thermally activated process between the excited states.[49]

As the light intensity of Cr^{3+} ions decreases with increasing temperature, the color of the CMGO luminophores is believed to change under UV excitation. In other words, the color of the luminophores can be modified by temperature control. In order to further study the color change visually, we note that when the temperature gradually increases from 298 K to 450 K, the color of our samples changes significantly from violet to red and the brightness continues to decrease. Reflecting the good stability of the Cr^{3+} ion, the results indicate that the temperature can be qualitatively determined by observation of the thermal discoloration behavior (Fig. 4b).

The important advantage of using the intensity ratio as a measure of the temperature of a thermally coupled system is that the population of each level is directly proportional to the total population. This makes the luminescence intensity ratio independent of the excitation intensity, since a change in the total population due to a change in excitation will affect the population of each level to the same extent. Eqn (7) was used for the fitting of the experimental results.[50,51]

$$\mathrm{FIR} = A \times \exp\left(\frac{-B}{T}\right) + C \tag{7}$$

where, A, B and C are constants. T is the absolute temperature and C is a constant offset.

The thermal equilibrium for FIR (589/771) and FIR (704/771) thus suggests that the Cr^{3+} substitution in the Mg^{2+} octahedral site leads to the splitting of the ^2E state into two R lines due to the low symmetry site. The solid line in Fig. 5 shows the fit using eqn (7). In particular, the energy gap ΔE was computed as 1814.4 cm^{-1} and 2123.7 cm^{-1}. There was a good linear function between the two energy levels. These results strongly suggest that the sample of CMGO:0.01Cr^{3+} could be used to reflect the variation in temperature.

In order to estimate the thermometric sensitivity, the absolute sensitivity (S_a) and the relative sensitivity (S_r), which reflect the rate of variation of the FIR parameter with temperature, were quantified using the following equations:[52,53]

$$S_a = \left|\frac{\delta \mathrm{FIR}}{\delta T}\right| \quad S_r = \frac{1}{\mathrm{FIR}}\left|\frac{\delta \mathrm{FIR}}{\delta T}\right| \tag{8}$$

The S_r values obtained first increase at a temperature of 370 K and then decrease for FIR (589/771), while the S_r values decrease continuously for the FIR (I_{704}/I_{771}) of CMGO:0.01Cr^{3+}. For 405 nm excitation, the high values for S_r are 1.4% and 0.7% K^{-1}, respectively (Fig. 6).

As can be seen in Fig. S3 (ESI†), the experimental temperature of the uncertainty was carried out by measuring the 100 spectra at 298 K under similar conditions, as the operation of the sensor is additionally dependent on the estimation of the temperature resolution. The temperature resolution values are generally distributed in a Gaussian pattern around room temperature. In this case, the standard deviation is 0.1 K. In order

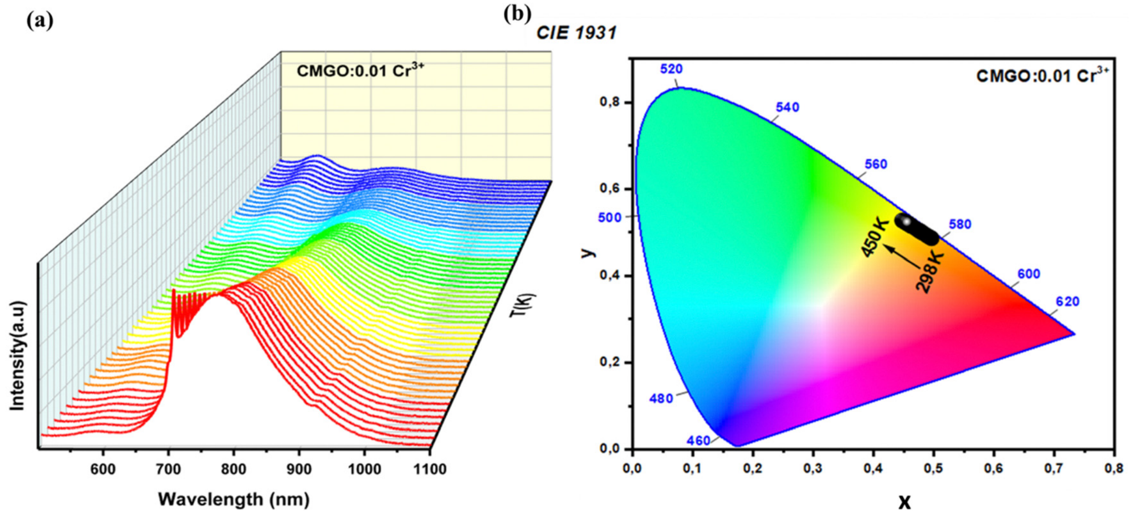

Fig. 4 (a) Temperature dependence of the PL emission spectra from 298 to 450 K. (b) CIE chromaticity diagram of the CMGO:0.01Cr^{3+} phosphor excited at various temperatures.

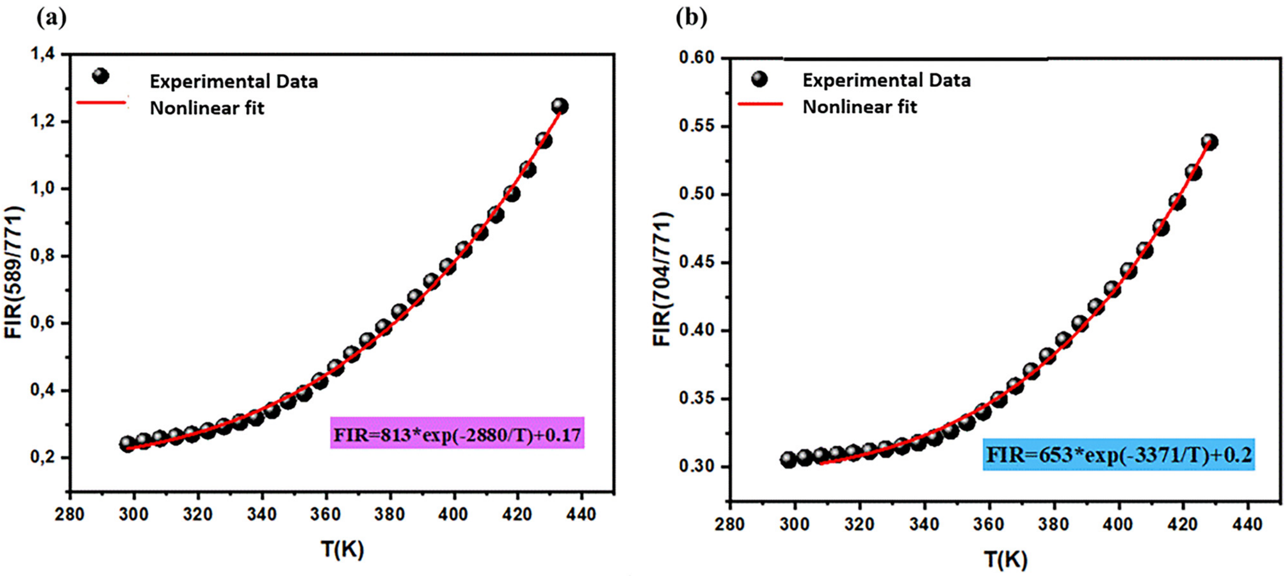

Fig. 5 FIR thermometry depending on CMGO:0.01Cr^{3+}. (a) FIR ($I_{589/771}$) and (b) FIR ($I_{704/771}$) in the studied range of temperature (298–450 K).

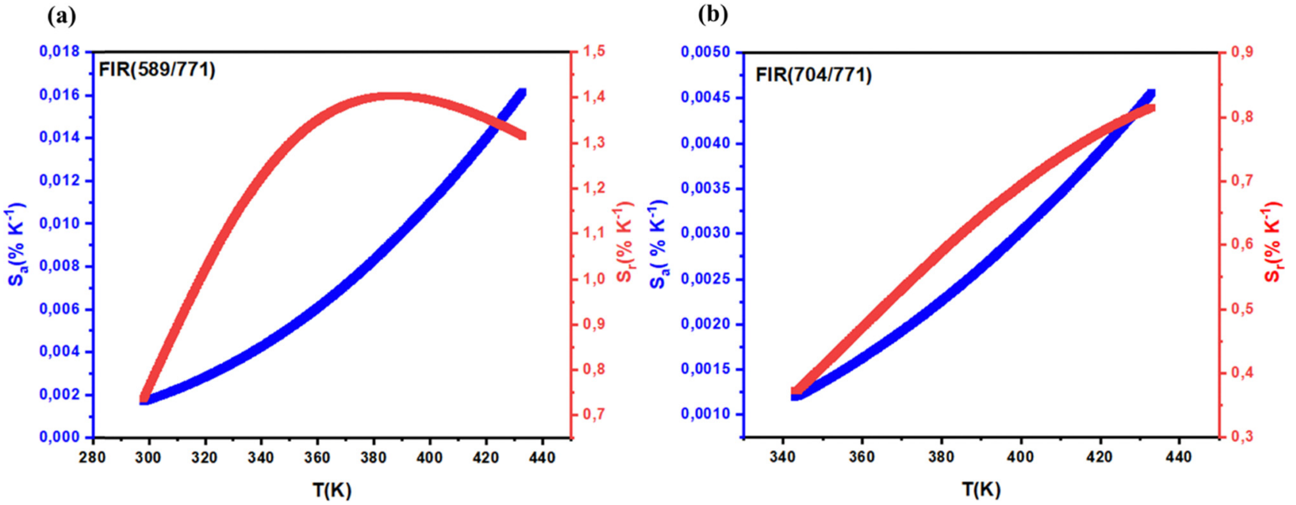

Fig. 6 The dependence of absolute sensitivity (S_a) and relative sensitivity (S_r) with temperatures of (a) I_{589}/I_{771} and (b) I_{704}/I_{771} for CMGO:0.01Cr^{3+}.

to evaluate the high temperature performance of different luminophores, we have summarized the maximum relative temperature sensitivities S_r at the highest temperature values for the luminescence thermometers, as shown in Table 1. These results highlight the potential of CMGO:0.01Cr^{3+} as an excellent candidate for optical temperature sensing applications, particularly in the context of multi-mode thermometry.

Table 1 Comparison of the temperature measurement performance of Cr^{3+}-doped radio metric thermometers

Materials	Temperature range (K)	S_r (% K^{-1})	T_m (K)	Ref.
α Ga_2O_3:Cr^{3+}	200–450	1.05	300	54
$Bi_2Ga_4O_9$:Cr^{3+}	80–600	0.7	90	42
$MgSiO_4$:Cr^{3+}	200–350	0.7	310	55
$Y_3Al_5O_{12}$:Cr^{3+}	123–573	0.55	384	56
$LiGa_5O_8$:Cr^{3+}	200–600	0.83	447	57
$LiGa_5O_8$:Cr^{3+}	300–463	0.59	386	58
Al_2O_3:Cr^{3+}	292–923	0.9	450	59
Ga_2O_3:Cr^{3+}	298–563	0.46	370	60
$ZnGa_2O_3$:Cr^{3+}	298–563	0.58	420	60
$CaMgGe_2O_6$:Cr^{3+}	298–450	1.4	390	This work

Temperature-dependent decay

The decay curve of the CMGO:0.01Cr^{3+} phosphor was obtained by excitation at 405 nm and monitoring the emission wavelength at 704 nm (Fig. 7a). The double exponential fit (DEF) is often used when the emission from optically active ions is localized in two different crystallographic positions from the point of view of local point symmetry. In this case, the DEF was used with a good correlation between the experimental decay and the fit. The lifetime values of the fast (τ_1) and slow (τ_2)

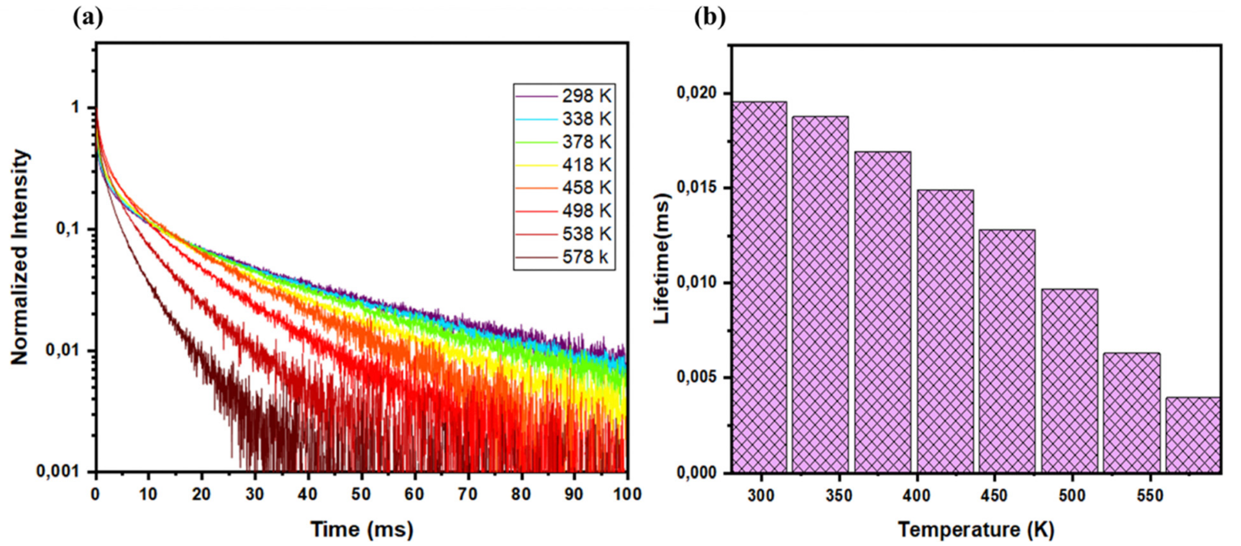

Fig. 7 (a) Decay profiles of CMGO:0.01Cr^{3+} measured in the range of temperature 298–578 K. (b) The average emission lifetime as a function of temperature.

components were determined using the following fitting formula, which describes the double exponential function:[61]

$$I = I_0 + A_1 e^{-(t-t_0)\tau_1} + A_2 e^{-(t-t_0)\tau_2} \tag{9}$$

where I_0 is the initial intensity of the luminescence, A_1 and A_2 are the pre-exponential factors, and $(t - t_0)$ is the difference between the initial time of the measurement after the excitation pulse t_0 and the time t.

The Cr^{3+} excitation lifetime is an average lifetime value based on the ^2E and $^4T_2$ excitation state population. As the temperature increases, the electrons gain enough energy to repopulate the higher $^4T_2$ state and the population of the $^4T_2$ state starts to increase and at the same time the population of the ^2E state starts to decrease. Thus, $^4T_2 \rightarrow {}^4A_2$ is dominant over $^2E \rightarrow {}^4A_2$. The decay rate of the ^2E state is slower than that of the $^4T_2$ state. Consequently, the lifetime decreases with increasing temperature.[62–64]

The emission lifetime reflects the decay of the excited state population of Cr^{3+} ions and decreases with increasing temperature due to enhanced non-radiative relaxation mechanisms as shown in Fig. 7b.

Two different environments have been occupied by the doped ions. Ions with shorter lifetimes (τ_1) are located at the surface or near the defect site and ions with longer lifetimes (τ_2) are situated in the center of the crystallite site and far from the defect site. In this context, the average lifetime was estimated using the formula:[65]

$$\tau = \frac{A_1\tau_1{}^2 + A_2\tau_2{}^2}{A_1\tau_1 + A_2\tau_2} \tag{10}$$

Since a low activation energy facilitates non-radiative quenching of the ^2E state, the results obtained are more or less in line with the expectations. An increase in temperature results in a progressive shortening of the lifetime, as can be seen for CMGO:0.01Cr^{3+} microcrystals (see Fig. 8a for other luminophores). This dependence is an indication that the microcrystals can be used for non-contact temperature detection. In order to quantify the observed thermal changes, the relative sensitivities (S_r) of the investigated LTs were determined according to the following formula:[66,67]

$$S_R = \frac{1}{X}\frac{\Delta X}{\Delta T}100\% \tag{11}$$

where X is the temperature related time parameter (in this case the mean decay time) and ΔX is the change in the X parameter with temperature change ΔT. The thermal evolution of the S_R, shown in Fig. 8b, reveals that a single maximum curve can be observed for almost all of the microcrystals studied. The value of the S_r maximum and the temperature of its occurrence depend on the host material and vary in the following way CMGO (2.5% K^{-1} at 578 K).

To analyze the performance of a sensor, one important parameter is required in addition to the sensitivity, which is called the temperature uncertainty or the minimum thermal resolution. This parameter can be estimated using the equation:[68]

$$\delta T = \frac{1}{S_r}\frac{\delta D}{D} \tag{12}$$

where δT is the uncertainty in the temperature, S_r is the relative sensitivity, and $\delta D/D$ is the uncertainty in the determination of the thermometric parameter (which has a specific value of 0.005 for any portable detector).[69,70] For the lifetime-based maximum sensitivity at 450 K, the uncertainty is evaluated to be 1.3 K (Fig. S4, ESI†).

The work presented in this article demonstrates that the use of Cr^{3+} dopants, each having a different quenching rate and energy flowing in the electronic level with little interference with each other, is an attractive way to design luminescence thermometers that operate over a wide temperature range.

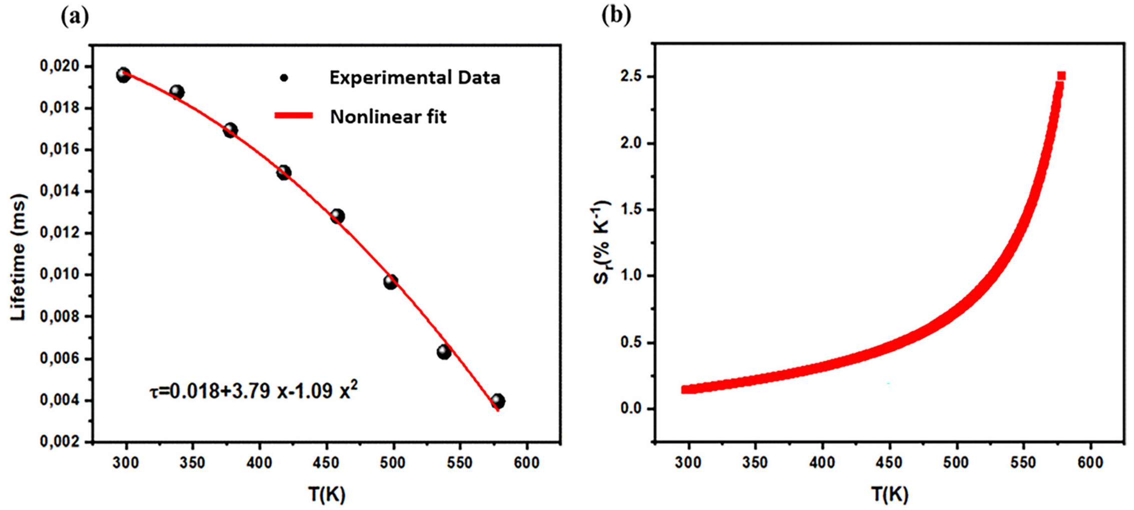

Fig. 8 (a) Thermal evolution of the mean decay times for Cr^{3+}-doped CMGO. (b) Relative sensitivities as a function of temperature.

Table 2 Comparison of relative sensitivities obtained for Cr^{3+} in different hosts using lifetime-based luminescent thermometers

Luminescent thermometer	$S_{r\,max}$ (% K^{-1})	T_{max} (K)	λ_{ex} (nm)	λ_{em} (nm)	Ref.
GC CaF_2:Cr^{3+}	0.47	573	464	1000	71
LaF_3:Er^{3+}, Yb^{3+}/Ga_2O_3:Cr^{3+}	0.66	500	400	720	72
GC Ga_2O_3:Cr^{3+}	0.46	370	406	687	73
CaF_2:Er^{3+}/$ZnAl_2O_4$:Cr^{3+}	0.67	535	396	690	74
$MgGa_2O_4$:Cr^{3+}	1.77	450	436	707	49
$ZnGa_2O_4$:Cr^{3+}	1.84	450	436	696	75
$Bi_2Al_4O_9$:Cr^{3+}	2.13	550	600	705	66
$CaMgGe_2O_6$:Cr^{3+}	2.5	578	405	704	This work

Using this approach, a CMGO:0.01Cr^{3+} phosphor thermometer has been developed with an exceptional operating range of 298 → 578 K, with reasonable S_r values over this range while preserving reasonable thermal resolution.

Table 2 shows that the sensitivity of our samples is higher than the values reported so far in other host materials. It is evident from the comparative analysis, that the CMGO:0.01Cr^{3+} phosphor synthesized in this work exhibits unique thermometric properties in the temperature range of 298–578 K. In particular, it has an exceptionally high relative sensitivity ($S_{r\,max}$) of 2.5 K^{-1}. This $S_{r\,max}$ value is higher than that of any of the other materials in the comparison and makes it particularly promising for applications where high temperature resolution and accuracy are required. The combination of a moderate temperature range, improved relative sensitivity and stable luminescence intensity make CMGO:0.01Cr^{3+} a competitive candidate for advanced optical thermometry applications where high accuracy is critical.

Conclusion

The Cr^{3+}-doped $CaMgGe_2O_6$ (CMGO:0.01Cr^{3+}) phosphors were successfully synthesized using a microparticle-enhanced solid-state method. X-Ray diffraction (XRD) confirmed the formation of a phase-pure monoclinic structure with high crystallinity. The luminescence properties were found to be strongly temperature-dependent, primarily governed by the spin-forbidden $^2E_g \rightarrow {}^4A_{2g}$ and spin-allowed $^4T_{2g} \rightarrow {}^4A_{2g}$ transitions of Cr^{3+}, enabling highly precise optical thermometry. This study highlights the importance of a dual-mode thermometric approach, combining fluorescence intensity ratio (FIR) and fluorescence lifetime (FL) techniques to enhance calibration accuracy and measurement reliability.

The self-referenced luminescence thermometry achieved by FIR (I_{589}/I_{771}) demonstrated a high relative sensitivity of 1.4% K^{-1} at 390 K, with an exceptionally low temperature uncertainty (δT = 0.11 K), making it a reliable method for precise temperature detection. More importantly, the integration of FL thermometry significantly improved the performance, achieving a maximum relative sensitivity of 2.5% K^{-1} at 578 K, along with the lowest temperature uncertainty of 1.3 K. The synergy between FIR and FL not only enhances sensitivity (S_r, S_a) but also refines the precision of the optical thermometer, addressing critical challenges in temperature sensing. These results establish Cr^{3+}-doped CMGO as a promising alternative to lanthanide-based phosphors, providing an efficient and cost-effective solution for luminescence thermometry. By demonstrating the feasibility of Cr^{3+}-activated phosphors for dual-mode thermometry, this work paves the way for further advances in transition metal-based optical temperature sensors and promotes their integration into next-generation high-precision thermal sensing applications.

Data availability

All data underlying the results are available as part of the article and no additional source data are required.

Conflicts of interest

There are no conflicts to declare.

References

1 M. Dramićanin, Lanthanide and transition metal ion doped materials for luminescence temperature sensing, *Luminescence Thermometry*, Elsevier, 2018, pp. 113–157.

2 J. Xue, Z. Yu, H. M. Noh, B. R. Lee, B. C. Choi, S. H. Park, J. H. Jeong, P. Du and M. Song, Designing multi-mode optical thermometers via the thermochromic $LaNbO_4:Bi^{3+}/Ln^{3+}$ (Ln = Eu, Tb, Dy, Sm) phosphors, *Chem. Eng. J.*, 2021, **415**, 128977.

3 P. Du, J. Tang, W. Li and L. Luo, Exploiting the diverse photoluminescence behaviors of $NaLuF_4:xEu^{3+}$ nanoparticles and g-C_3N_4 to realize versatile applications in white light-emitting diode and optical thermometer, *Chem. Eng. J.*, 2021, **406**, 127165.

4 D. Chrétien, P. Bénit, H.-H. Ha, S. Keipert, R. El-Khoury, Y.-T. Chang, M. Jastroch, H. T. Jacobs, P. Rustin, M. Rak and N. Lane, Mitochondria are physiologically maintained at close to 50 °C, *PLoS Biol.*, 2018, **16**(1), e2003992.

5 S. Kiyonaka, R. Sakaguchi, I. Hamachi, T. Morii, T. Yoshizaki and Y. Mori, Validating subcellular thermal changes revealed by fluorescent thermosensors, *Nat. Methods*, 2015, **12**(9), 801–802.

6 Y. Bahrouni, I. Kachou, K. Saidi, T. Kallel, M. Dammak and I. Mediavilla Jiménez, Enhancing Luminescence Intensity of Eu^{3+}-Activated $NaYb(MoO_4)_2$ Phosphors through Bismuth Doping: Judd-Ofelt Analysis, Lighting, and Temperature-Sensing Applications, *Mater. Adv.*, 2025, **6**(4), 1307–1318.

7 G. Wei, P. Li, R. Li, Y. Wang, S. He, J. Li, Y. Shi, H. Suo, Y. Yang and Z. Wang, How to Achieve Excellent Luminescence Properties of Cr Ion-Doped Near-Infrared Phosphors, *Adv. Optical Mater.*, 2023, **11**, 2301794.

8 N. Ahmed, H. Kraus, H. J. Kim, V. Mokina, V. Tsiumra, A. Wagner, Y. Zhydachevskyy and V. B. Mykhaylyk, Characterisation of tungstate and molybdate crystals ABO_4 (A = Ca, Sr, Zn, Cd; B = W, Mo) for luminescence lifetime cryothermometry, *Materialia*, 2018, **4**, 287–296.

9 X. F. Wang, Q. Liu, Y. Y. Bu, C. S. Liu, T. Liu and X. H. Yan, Optical temperature sensing of rare-earth ion doped phosphors, *RSC Adv.*, 2015, **5**, 86219–86236.

10 M. D. Dramićanin, B. Milićević, V. Đorđević and Z. Ristić, $Li_2TiO_3:Mn^{4+}$ Deep-Red Phosphor for the Lifetime-Based Luminescence Thermometry, *ChemistrySelect*, 2019, **4**, 7067–7075.

11 D. Chen, X. Chen, X. Li, H. Guo, S. Liu and X. Li, Cr^{3+}-doped $Bi_2Ga_4O_9$-$Bi_2Al_4O_9$ solid-solution phosphors: crystal-field modulation and lifetime-based temperature sensing, *Opt. Lett.*, 2017, **42**, 4950–4953.

12 J. Zhang, Y. Zhang and X. Jiang, Investigations on upconversion luminescence of $K_3Y(PO_4)_2:Yb^{3+}$-$Er^{3+}/Ho^{3+}/Tm^{3+}$ phosphors for optical temperature sensing, *J. Alloys Compd.*, 2018, **748**, 438–445.

13 M. Prasad and V. K. Rai, Thermally stable upconverting $Na_3Zr_2(SiO_4)_2PO_4:Er^{3+}/Yb^{3+}$ phosphors for displays and optical thermometry, *J. Alloys Compd.*, 2022, **911**, 164968.

14 C. Li, B. Chen, D. Deng, M. Wu, H. Yu, H. Li, C. Shen, L. Wang and S. Xu, Ratiometric optical thermometer with high-sensitive temperature sensing based on synergetic luminescence of Ce^{3+}-Eu^{2+} in $LiSr_4(BO_3)_3$ phosphors, *J. Alloys Compd.*, 2020, **838**, 155675.

15 S. Zhu, D. Zhao, R. Zhang, Q. Yao and W. Liu, Study on energy transfer and temperature sensing properties of Pb^{2+}/Sm^{3+} co-doped $Ba_2MgY_2(BO_3)_4$, *Ceram. Int.*, 2023, **49**, 18654–18661.

16 S. P. Singh, M. Kim, W. B. Park, J. W. Lee and K. S. Sohn, Discovery of a red-emitting $Li_3RbGe_8O_{18}:Mn^{4+}$ phosphor in the alkali-germanate system: structural determination and electronic calculations, *Inorg. Chem.*, 2016, **55**, 10310–10319.

17 Q. Huang, W. Ye, G. Hu and X. Liu, Strong red emission in Bi^{3+} and Mn^{4+} codoped $Mg_{3.5}Ge_{1.25}O_6$ phosphors applied in optical agriculture, *J. Lumin.*, 2019, **210**, 89–95.

18 Q. Bai, Z. Wang, P. Li, T. Li, S. Xu and Z. Yang, Luminescence properties of novel deep-red-emitting $Ca_3Al_2Ge_2O_{10}:Cr^{3+}$ phosphors, *Luminescence*, 2016, **31**, 1277–1282.

19 K. Thejas, M. Abraham, A. Kunti, M. Tchernychev, S. Ahmad and S. Das, Review on deep red-emitting rare-earth-free germanates and their efficiency as well as adaptability for various applications, *Appl. Mater. Today*, 2021, **24**, 101094.

20 P. Li, L. Wondraczek, M. Peng, Q. Zhang and A. Setlur, Tuning Mn^{4+} red photoluminescence in $(K,Rb)_2Ge_4O_9:Mn^{4+}$ solid solutions by partial alkali substitution, *J. Am. Ceram. Soc.*, 2016, **99**, 3376–3381.

21 J. Kunitomo, R. Suzuki, Y. Takahashi, T. Miyazaki, N. Terakado and T. Fujiwara, Red-emissive Mn-doped $Li_2Ge_4O_9$ phase synthesized via glass-ceramic route, *J. Ceram. Soc. Jpn.*, 2014, **122**, 725–727.

22 J. Xue, W. Ran, H. M. Noh, B. C. Choi, S. H. Park, J. H. Jeong and J. H. Kim, Influence of alkaline ions on the luminescent properties of Mn^{4+}-doped MGe_4O_9 (M = Li_2, LiNa and K_2) red-emitting phosphors, *J. Lumin.*, 2017, **192**, 1072–1083.

23 H. Zeng, T. Zhou, L. Wang and R.-J. Xie, *Chem. Mater.*, 2019, **31**, 5245.

24 J. Qiao, G. Zhou, Y. Zhou, Q. Zhang and Z. Xia, *Nat. Commun.*, 2019, **10**, 5267.

25 W.-T. Huang, C.-L. Cheng, Z. Bao, C.-W. Yang, K.-M. Lu, C.-Y. Kang, C.-M. Lin and R.-S. Liu, *Angew. Chem., Int. Ed.*, 2019, **58**, 2069.

26 L. Chen, S. Yu, G. Shen, S. Tang, T. Zhang, J. Li and Q. Zhu, Large-scale irrigation of Cr^{3+} into different octahedra of zinc aluminate toward continual broadband near-infrared emission, *Ceram. Int.*, 2024, **50**, 1956–1969.

27 L. Chen, P. Li, G. Shen, X. Kang, S. Tang, T. Zhang and Q. Zhu, Effective electron trap regulation in near-infrared persistent phosphor of $ZnAl_2O_4:Cr^{3+}$ for round-the-clock plant lighting, *Mater. Today Chem.*, 2024, **40**, 102204.

28 L. Fang, L. Zhang, H. Wu, H. Wu, G. Pan, Z. Hao, F. Liu and J. Zhang, Efficient Broadband Near-Infrared $CaMgGe_2O_6:Cr^{3+}$ Phosphor for pc LED, *Inorg. Chem.*, 2022, **61**, 8815–8822.

29 L. Bellucci, M. Cassetta, H. Skogby and S. Nazzareni, Pure and Sc-Doped Diopside ($CaMgSi_2O_6$) Vibrational Spectra:

Modelling and Experiments, *Phys. Chem. Chem. Phys.*, 2024, **26**, 4029–4038.

30 R. D. Shannon, Revised effective ionic radii and systematic studies of interatomic distances in halides and chalcogenides, *Acta Crystallogr., Sect. A: Found. Crystallogr.*, 1976, **32**, 751–767.

31 M. Akasaka, Y. Takasu, M. Handa, M. Nagashima, M. Hamada and T. Ejima, Distribution of Cr^{3+} between octahedral and tetrahedral sites in synthetic blue and green $(CaMgSi_2O_6)_{95}$ $(CaCrAlSiO_6)_5$ diopsides, *Mineral. Mag.*, 2019, **83**, 497–505.

32 Q. Wu, P. L. Li, Z. J. Ye, X. X. Huo, H. F. Yang, Y. Wang, D. W. Wang, J. X. Zhao, Z. P. Yang and Z. J. Wang, Near-infrared emitting phosphor $LaMg_{0.5}(SnGe)_{0.5}O_3$:$Cr^{3+}$ for plant growth applications: crystal structure, luminescence, and thermal stability, *Inorg. Chem.*, 2021, **60**, 16593–16603.

33 Q. Wang, S. W. Wang, T. Tan, J. T. Wang, R. Pang, D. Li, C. Y. Li and H. J. Zhang, Efficient Cr^{3+}-activated $NaInP_2O_7$ phosphor for broadband near-infrared LED applications, *Inorg. Chem. Front.*, 2022, **9**, 3692–3701.

34 K. Saidi, C. Hernández-Álvarez and M. Runowski, *et al.*, Ultralow pressure sensing and luminescence thermometry based on the emissions of Er^{3+}/Yb^{3+} codoped $Y_2Mo_4O_{15}$ phosphors, *Dalton Trans.*, 2023, **52**, 14904–14916.

35 M. Vasile, P. Vlazan and N. M. Avram, Characterization and optical properties of $ZnGa_2O_4$:Eu^{3+} nanophosphor grown by hydrothermal method, *J. Alloys Compd.*, 2010, **500**, 185–189.

36 L. Xi, L. Pan, Y. Wang and P. D. Townsend, The influence of doped Cr ions on the luminescence properties of infrared long persistent phosphor $ZnAl_2O_4$ with the substitution of Ge ions, *J. Lumin.*, 2021, **233**, 117941.

37 Y. Zhang, R. Huang, H. L. Li, D. J. Hou, Z. X. Lin, J. Song, Y. Z. Guo, H. H. Lin, C. Song, Z. W. Lin and J. Robertson, Germanium substitution endowing Cr^{3+}-doped zinc aluminate phosphors with bright and super-long near-infrared persistent luminescence, *Acta Mater.*, 2018, **155**, 214–221.

38 A. Mondal and J. Manam, Structural, optical and temperature-dependent photoluminescence properties of Cr^{3+}-activated $LaGaO_3$ persistent phosphor for optical thermometry, *Ceram. Int.*, 2020, **46**, 25601.

39 N. Basavaraju, K. R. Priolkar, D. Gourier, S. K. Sharma, A. Bessière and B. Viana, The importance of inversion disorder in the visible light-induced persistent luminescence in Cr^{3+} doped AB_2O_4 (A = Zn or Mg and B = Ga or Al), *Phys. Chem. Chem. Phys.*, 2015, **17**, 1790–1799.

40 Q. Zhu, J. Q. Xiahou, X. D. Li, X. D. Sun and J. G. Li, Defect cluster engineering in $ZnGa_{2-x}(Mg/Ge)_xO_4$:Cr^{3+} nanoparticles for remarkably improved NIR persistent luminescence, *J. Am. Ceram. Soc.*, 2021, **104**, 4594–4605.

41 T. Narendrudu, S. Suresh, G. C. Ram, N. Veeraiah and D. K. Rao, Spectroscopic and structural properties of Cr^{3+} ions in lead niobium germanosilicate glasses, *J. Lumin.*, 2017, **183**, 172–179.

42 M. Back, E. Trave, J. Ueda and S. Tanabe, Ratiometric optical thermometer based on dual near-infrared emission in Cr^{3+}-doped bismuth-based gallate host, *Chem. Mater.*, 2016, **28**, 8347–8356.

43 C. X. Yuan, R. Y. Li, Y. F. Liu, L. L. Zhang, J. H. Zhang, G. Leniec, P. Sun, Z. H. Liu, Z. H. Luo, R. Dong and J. Jiang, Efficient and broadband $LiGaP_2O_7$:Cr^{3+} phosphors for smart near-infrared light-emitting diodes, *Laser Photonics Rev.*, 2021, **15**, 2100227.

44 J. Yang, Y. X. Liu, Y. Y. Zhao, Z. Gong, M. Zhang, D. T. Yan, H. C. Zhu, C. G. Liu, C. S. Xu and H. Zhang, Ratiometric afterglow nanothermometer for simultaneous in situ bioimaging and local tissue temperature sensing, *Chem. Mater.*, 2017, **29**, 8119–8131.

45 Y. Li, Y. Y. Li, R. C. Chen, K. Sharafudeen, S. F. Zhou, M. Gecevicius, H. H. Wang, G. P. Dong, Y. L. Wu, X. X. Qin and J. R. Qiu, Tailoring of the trap distribution and crystal field in Cr^{3+}-doped non-gallate phosphors with near-infrared long-persistence phosphorescence, *NPG Asia Mater.*, 2015, **7**, e180.

46 Y. Y. Zhan, Y. H. Jin, H. Y. Wu, L. F. Yuan, G. F. Ju, Y. Lv and Y. H. Hu, Cr^{3+}-doped $Mg_4Ga_4Ge_3O_{16}$ near-infrared phosphor membrane for optical information storage and recording, *J. Alloys Compd.*, 2019, **777**, 991–1000.

47 H. H. Lin, G. X. Bai, T. Yu, M. K. Tsang, Q. Y. Zhang and J. H. Hao, Site occupancy and near-infrared luminescence in $Ca_3Ga_2Ge_3O_{12}$:Cr^{3+} persistent phosphor, *Adv. Opt. Mater.*, 2017, **5**, 1700227.

48 V. Mykhaylyk, H. Kraus, Y. Zhydachevskyy, V. Tsiumra, A. Luchechko, A. Wagner and A. Suchocki, Multimodal Non-Contact Luminescence Thermometry with Cr-Doped Oxides, *Sensors*, 2020, **20**, 5259.

49 A. Mondal and J. Manam, Investigations on spectroscopic properties and temperature-dependent photoluminescence of Cr^{3+} doped $MgGa_2O_4$ phosphor, *Mater. Res. Express*, 2019, **6**, 095081.

50 L. Marciniak, M. Szalkowski, A. Bednarkiewicz and K. E. Piecka, A Cr^{3+} luminescence-based ratiometric optical laser power meter, *J. Mater. Chem. C*, 2022, **10**, 11040–11047.

51 M. Fhoula, K. Saidi, C. H. Álvarez, K. S. Carracedo, M. Dammak and I. R. Martín, Unlocking the luminescent potential of Pr^{3+}/Yb^{3+} Co-doped $Y_2Mo_4O_{15}$ for advanced thermometry applications, *J. Alloys Compd.*, 2024, **979**, 173537.

52 I. Kachou, M. Dammak, S. Auguste, F. Amiard and P. Daniel, A novel optical temperature sensor and energy transfer properties based on Tb^{3+}/Sm^{3+} codoped $SrY_2(MoO_4)_4$ phosphors, *Dalton Trans.*, 2023, **52**, 18233–18246.

53 C. D. S. Brites, P. P. Lima, N. J. O. Silva, A. Millán, V. S. Amaral, F. Palacio and L. D. Carlos, Thermometry at the Nanoscale, *Nanoscale*, 2012, **4**, 4799–4829.

54 M. Back, E. Trave, J. Ueda and S. Tanabe, *Chem. Mater.*, 2016, **28**, 8347.

55 Z. Ristić, V. Đorđević, M. Medić, S. Kuzman, M. Sekulić, Ž. Antić and M. D. Dramićanin, *Meas. Sci. Technol.*, 2021, **32**, 054004.

56 K. Elzbieciak and L. Marciniak, *Front. Chem.*, 2018, **6**, 424.

57 X. Li, G. Jiang, S. Zhou, X. Wei, Y. Chen, C. K. Duan and M. Yin, *Sens. Actuators, B*, 2014, **202**, 1065.

58 D. Chen, S. Liu, W. Xu and X. Li, *J. Mater. Chem. C*, 2017, **5**, 11769.

59 A. Ćirić, S. Stojadinović, Z. Ristić, Ž. Antić and M. D. Dramićanin, *Sens. Actuators, A*, 2021, **331**, 112987.

60 D. Chen, Z. Wan, Y. Zhou and Z. Ji, *J. Eur. Ceram. Soc.*, 2015, **35**, 4211.

61 K. E. Piecka, J. Drabik, D. Jaque and L. Marciniak, Cr^{3+}-based nanocrystalline luminescent thermometers operating in a temporal domain, *Phys. Chem. Chem. Phys.*, 2020, **22**, 22555–22564.

62 B. Malysa, A. Meijerink, W. Wu and T. Jüstel, On the influence of calcium substitution to the optical properties of Cr^{3+} doped $SrSc_2O_4$, *J. Lumin.*, 2017, **190**, 234–241.

63 M. Jong, L. Seijo, A. Meijerink and F. T. Rabouw, Resolving the ambiguity in the relation between Stokes shift and Huang-Rhys parameter, *Phys. Chem. Chem. Phys.*, 2015, **17**, 16959–16969.

64 E. Glais, M. Pellerin, V. Castaing, D. Alloyeau, N. Touati, B. Viana and C. Chaneac, Luminescence properties of $ZnGa_2O_4$:Cr^{3+}, Bi^{3+} nanophosphors for thermometry applications, *RSC Adv.*, 2018, **8**, 41767–41774.

65 X. Xu, J. R. G. Chen, D. Kong, C. Gu, C. Chen and L. Kong, Bright green emission from the Mn^{2+}-doped zinc gallogermanate phosphors, *Opt. Mater. Express*, 2013, **3**, 1727–1732.

66 D. Chen, X. Chen, X. Li, H. Guo, X. Liu and X. Li, Cr^{3+}-doped $Bi_2Ga_4O_9$-$Bi_2Al_4O_9$ solid solution phosphors: crystal-field modulation and lifetime-based temperature sensing, *Opt. Lett.*, 2017, **42**, 4950–4953.

67 S. Gharouel, L. Labrador-Páez, P. Haro-González, K. Horchani-Naifer and M. Férid, Fluorescence Intensity Ratio and lifetime thermometry of praseodymium phosphates for temperature sensing, *J. Lumin.*, 2018, **201**, 372–383.

68 J. A. Mares, G. Boulon, A. Brenier, L. Lou and S. R. Rotman, Spectroscopy of multisites Cr^{3+} and Nd^{3+} in yttrium aluminum perovskite, *Chem. Phys. Lett.*, 1994, **217**, 105–111.

69 P. R. Nelson, A. Brenier, C. Pedrini, G. Boulon and J. A. Mares, Chromium Neodymium energy transfer in YAP, *J. Phys. IV*, 1991, **1**, 257–262.

70 N. L. Ross, J. Zhao and R. J. Angel, High-pressure single-crystal X-ray diffraction study of $YAlO_3$ perovskite, *J. Solid State Chem.*, 2004, **177**, 1276–1284.

71 C. Wang, A. Wadhwa, S. Cui, R. Ma, X. Qiao, X. Fan and X. Zhang, Dual mode temperature sensing through luminescence lifetimes of F- and O-coordinated Cr^{3+} sites in fluorosilicate glass-ceramics, *RSC Adv.*, 2017, **7**, 52435–52441.

72 Z. Fang, L. Zhao, Q. Yang, Z. Yang, Y. Cai, D. Zhou, X. Yu, J. Qiu and X. Xu, Optical thermometry properties of silicate glass ceramics with dual-phase for spatial isolation of Er^{3+} and Cr^{3+}, *J. Lumin.*, 2020, **219**, 116861.

73 D. Chen, Z. Wan, Y. Zhou and Z. Ji, Cr^{3+}-doped gallium-based transparent bulk glass ceramics for optical temperature sensing, *J. Eur. Ceram. Soc.*, 2015, **35**, 4211–4216.

74 A. Wadhwa, C. Wang, C. Wang and R. Ma, Multi-phase glass-ceramics containing CaF_2:Er^{3+} and $ZnAl_2O_4$:Cr^{3+} nanocrystals for optical temperature sensing, *J. Am. Ceram. Soc.*, 2019, **102**, 2472–2481.

75 A. Mondal, S. Das and J. Manam, Investigation on spectroscopic properties and temperature-dependent photoluminescence of NIR emitting Cr^{3+} doped zinc gallate long persistent nanophosphor, *Physica B*, 2019, **569**, 20–30.